



2D porous nanosheets of Y-doped ZnO for dielectric and ferroelectric applications

Sahil Goel¹ · Nidhi Sinha² · Harsh Yadav¹ · Abhilash J. Joseph¹ · Binay Kumar¹

Received: 24 March 2018 / Accepted: 16 June 2018 / Published online: 22 June 2018
© Springer Science+Business Media, LLC, part of Springer Nature 2018

Abstract

Ferroelectricity in pure ZnO nanocrystals is an unlikely physical phenomenon. Here, we show origin of high temperature ferroelectricity in ZnO as a result of yttrium (Y) doping. First, we briefly introduced the wet chemical synthesis of pure and yttrium (Y) doped ZnO nanocrystals. The crystalline phase and morphological appearance of as synthesized pure and Y-doped ZnO nanocrystals were examined using powder X-ray diffraction (XRD), scanning electron microscopy (SEM) and transmission electron microscopy (TEM) techniques. By Y-doping, the morphology of ZnO crystals evolved from 1D nanopencil (pure ZnO) to 3D flower-like architectures assembled by 2D porous nanosheets (Y-ZnO). Crystallite size, deformation stress, energy density and lattice strain of both the nanoparticles were evaluated using Scherrer and Williamson-Hall methods. Frequency as well as temperature dependence of dielectric constant, dielectric loss and ac conductivity of Y-doped ZnO nanosheets were investigated. Ferroelectricity in Y-doped ZnO nanosheets was established using the temperature dependent curve of dielectric constant and the room temperature polarization hysteresis loop. The temperature dependent curve of dielectric constant displayed a ferroelectric to paraelectric transition peak at 138 °C. The Y-ZnO nanosheets exhibit weak ferroelectric polarization hysteresis loop with a remnant polarization (P_r) of 0.09 $\mu\text{C}/\text{cm}^2$ and a coercive field (E_c) of 5.87 kV/cm (@ RT). The nature of the leakage present in Y-ZnO sample was extracted from the time-dependent compensated (TDC) hysteresis study. Leakage current density was found to decrease due to Y-doping in ZnO nanocrystals.

1 Introduction

1.1 Overview

Highly polarizable binary compounds with off-centered ions were found to display ferroelectric characteristics at low temperatures [1]. In particular, the narrow energy gap (~ 0.2 eV) IV–VI binary compounds, like $\text{Pb}_{1-x}\text{Ge}_x\text{Te}$, have attracted considerable attention thanks to their low temperature ferroelectric phase. It has been well established that the ferroelectricity in $\text{Pb}_{1-x}\text{Ge}_x\text{Te}$ originates as a result

of ordering in the off centered Ge ions [2, 3]. Moreover, a similar ferroelectric phase transition was discovered in II–VI semiconductors such as $\text{Zn}_{1-x}\text{Cd}_x\text{Te}$ [4, 5] and $\text{Zn}_{1-x}\text{Li}_x\text{O}$ [6] as a result of ordering of off-centered dopant ions. Zinc oxide, ZnO, being a II–VI binary compound possesses a much stronger ionic character, when compared to IV–VI binary compounds [7].

ZnO is an n-type II–VI piezoelectric semiconductor [8]. Because of its excellent piezoelectric and electro-mechanical characteristics, ZnO has been successfully employed in wide range of practical applications such as surface acoustic wave (SAW) devices, ultrasonic transducers, gas sensors and mechanical energy harvesters [9–15]. ZnO exhibits a hexagonal wurtzite crystal structure ($p6_3mc$). Furthermore, the wurtzite structure is polar along the ‘c’ crystallographic axis and the tetrahedrally coordinated Zn^{2+} and O^{2-} ions are alternatively stacked along this c-polar axis. No phase transition has been observed in pure ZnO crystal at atmospheric pressure. Pure ZnO is a polar crystal and it is not possible to reverse its electric dipole moment by reversing the direction of applied external electric field, which explains its non-ferroelectric character. A ferroelectric phase transition was

Electronic supplementary material The online version of this article (<https://doi.org/10.1007/s10854-018-9513-2>) contains supplementary material, which is available to authorized users.

✉ Binay Kumar
b3kumar69@yahoo.co.in

¹ Crystal Lab, Department of Physics & Astrophysics, University of Delhi, Delhi 110007, India

² Department of Electronics, SGTB Khalsa College, University of Delhi, Delhi 110007, India

first observed in Li doped ZnO by several research groups [6, 16–18]. The large mismatch between the ionic radii of the host Zn^{2+} (0.74 Å) ion and the dopant Li^{2+} (0.60 Å) ions and the ordering of the off-centered Li^{2+} dopant ions were considered to play a crucial role in the appearance of ferroelectricity. The direction of spontaneous polarization (P_s) is unique in wurtzite ZnO ('*c*'-axis), whereas eight ferroelectric domains are allowed in rhombohedral $\text{Pb}_{1-x}\text{Ge}_x\text{Te}$ and $\text{Cd}_{1-x}\text{Zn}_x\text{Te}$; this makes ZnO advantageous over other binary semiconductors and thus, it is a material of choice for ferroelectric integrated devices.

ZnO is not a ferroelectric material in its pure form. However, doping is considered as a very common approach for introducing ferroelectricity in ZnO. For instance, A. Onodera et al. have synthesized the $\text{Zn}_{1-x}\text{Li}_x\text{O}$ and $\text{Zn}_{1-x}(\text{Li}_{0.02}\text{Mg}_{x-0.02})\text{O}$ ceramics and reported a ferroelectric transition around 57 °C for $\text{Zn}_{0.9}\text{Li}_{0.1}\text{O}$, and at 87 °C for $\text{Zn}_{0.7}(\text{Li}_{0.02}\text{Mg}_{0.28})\text{O}$ [16, 17]. The spontaneous polarization (P_s) of $\text{Zn}_{0.7}(\text{Li}_{0.02}\text{Mg}_{0.28})\text{O}$ ceramic sample was found to be 0.02 $\mu\text{C}/\text{cm}^2$ at 40 °C. Yang et al. [19] found Cr-doped ZnO to be ferroelectrically active with a remnant polarization $\sim 0.2 \mu\text{C}/\text{cm}^2$ and a coercive field $\sim 50 \text{ kV}/\text{cm}$ (@ 2 kHz). G. Srinet et al. [20] synthesized Ba (5%) doped ZnO nanoparticles (NPs) and observed the ferroelectric to paraelectric phase transition (T_c) at 330 °C with remnant polarization (P_r) and coercive field (E_c) equal to 1.01 $\mu\text{C}/\text{cm}^2$ and 2.02 kV/cm, respectively. Yang et al. [21] prepared 9 at% Cr-doped ZnO thin films and observed a ferroelectric to paraelectric phase transition at 95 °C with a remnant polarization and coercive field of $\sim 0.4 \mu\text{C}/\text{cm}^2$ and $\sim 80 \text{ kV}/\text{cm}$, respectively.

1.2 Scope of this article

Interestingly, in our previous works we have successfully discovered the ferroelectric nature in rare earth doped ZnO nanostructures, namely, Eu^{3+} doped ZnO ($T_c = 230 \text{ }^\circ\text{C}$; $P_r = 0.11 \mu\text{C}/\text{cm}^2$ and $E_c = 5.81 \text{ kV}/\text{cm}$), Gd^{3+} doped ZnO ($T_c = 215 \text{ }^\circ\text{C}$; $P_r = 0.29 \mu\text{C}/\text{cm}^2$ and $E_c = 16.41 \text{ kV}/\text{cm}$) and La^{3+} doped ZnO ($T_c = 276 \text{ }^\circ\text{C}$; $P_r = 0.027 \mu\text{C}/\text{cm}^2$ and $E_c = 1.33 \text{ kV}/\text{cm}$) nanorods (NRs) [22–24]. This article is a part of our ongoing interest on the search of ferroelectricity with high ferro- to para-electric transition temperature as a result of rare earth doping in ZnO [22–25]. Very recently, we have reported a gigantic piezoelectric response ($d_{33} \sim 420 \text{ pm}/\text{V}$) for yttrium (Y^{3+}) doped ZnO nanosheets (NSs) and have successfully generated an output voltage of around 20 V from Y-ZnO NSs based nanogenerator (NG). The Y-ZnO NSs were demonstrated to be a potential material for powering various self-powered devices [26].

In the present report, growth of Y-doped ZnO NSs by wet-chemical co-precipitation method was pursued in order to investigate its applicability in the ferroelectric devices. The structural and morphological properties of the Y-doped

ZnO NSs were studied in detail using XRD and TEM & SEM analysis, respectively. The numerical values of crystallite size, lattice strain, deformation stress and deformation energy density for both pure and Y-doped NPs were evaluated using Scherrer, W-H and FESEM and TEM methods. We discovered a striking ferroelectric phenomenon in Y-doped ZnO NSs that is attributed to the difference in the ionic radii of dopant Y^{3+} ion (1.04 Å) and host Zn^{2+} (0.74 Å) ion. Due to this mismatch in ionic radii between host and the dopant, Y atoms can occupy off-centered positions, forming permanent local electric dipoles, which can easily be reversed on changing the direction of applied electric field and thereby resulting in ferroelectric characteristics. Such a conclusion was further confirmed by measuring the dielectric constant as a function of temperature. Further, till now, to the best of our knowledge there are no reports available on dielectric, ferroelectric studies of Y doped ZnO nanosheets.

2 Experimental details

2.1 Materials

The commercially available (AR grade; Merck) sodium hydroxide; NaOH, zinc chloride; ZnCl_2 , yttrium(III) chloride hexahydrate; $\text{YCl}_3 \cdot 6\text{H}_2\text{O}$, ethanol; $\text{C}_2\text{H}_5\text{OH}$ and doubly distilled water were used for the synthesis of pure and Y-doped ZnO NPs.

2.2 Nanoparticles synthesis

Pure and (5 mol%) Y-doped ZnO NPs were prepared by a wet-chemical co-precipitation method.

2.2.1 Preparation of pure-ZnO nanoparticles

To prepare ZnO NPs, ZnCl_2 and NaOH were taken as the starting materials in a molar ratio of 1:7. In a typical procedure, 0.05 mol of ZnCl_2 was dissolved in 100 ml of doubly distilled water with a continuous stirring for a hour, making precursor solution A. Then, another precursor solution B was made by dissolving 0.35 mol of NaOH in 100 ml of doubly distilled water with a continuous stirring for 60 min. The above obtained solution B was poured drop wise into solution A under constant stirring for 30 min to obtain a milky solution containing ZnO precipitate. The white precipitated powder was washed several times with ethanol and doubly distilled water to remove sodium ions, chloride ions and impurities. Now, the as obtained white precipitate was dried at 80 °C for 6 h and then it was calcinated at 500 °C for 3 h.

2.2.2 Preparation of Y-doped ZnO nanoparticles

To synthesize Y-doped ZnO NPs, the procedure described above was repeated. In the synthesis procedure of Y-ZnO, yttrium(III) chloride hexahydrate (5 mol% with respect to ZnCl_2) was dissolved in 50 ml of doubly distilled water. This solution was then added to the solution of ZnCl_2 . In order to prepare Y-ZnO NPs, solution of NaOH was added drop by drop to the above prepared solution under a constant stirring for 60 min. The obtained Y-ZnO precipitate was washed several times with ethanol and then dried at 90 °C for 6 h. At last, the precipitated powder was heat treated at 550 °C for 3 h.

2.3 Characterization techniques

The structural and crystallographic characterizations of pure and Y-doped ZnO samples were performed using high resolution X-ray diffractometer (Make: Bruker, Model: D8 Discover) with Cu K_α radiation of wavelength 1.5408 Å. The external morphology (shape and size) of these samples were investigated using transmission electron microscopy (TEM) on a FEI Netherlands instrument (Model: Technai G²T30) and field emission scanning electron microscopy (FESEM) on a TESCAN instrument (Model: MIRA3LMH). The dielectric properties of the pelletized sample of Y-ZnO powder were measured using a Broadband Dielectric/Impedance Analyzer (Make: Novocontrol Germany, Model: C-50 Alpha A) in a frequency range 100 Hz–1 MHz and with temperature range 35–200 °C. The ferroelectric P–E loops of as-synthesized Y-doped ZnO NSs were recorded at a frequency of 500 Hz in Sawyer–Tower mode with the help of a Precision LC Ferroelectric tester (Make: Radiant technologies,

Model: P-HVi210KSC). I–V characteristics of both pure and Y-ZnO NPs were also studied using Radiant technologies instrument (Model: P-HVi210KSC).

3 Results and discussions

3.1 Analysis of crystal structure and composition

Figure 1a depicts the room temperature XRD patterns of pure and Y-doped ZnO NPs. The positions of all the diffraction peaks for both the NPs matched well with the hexagonal ZnO wurtzite phase (standard JCPDS card No. 36-1451). Diffraction peaks that could be related to Y-containing phases and impurity phases were not detected, indicating the fact that the Y^{3+} dopant ions have been successfully incorporated into Zn^{2+} host ion sites in the ZnO lattice. The crystalline peaks intensity got decreased and were slightly broadened due to the presence of Y-dopant. The most intense Bragg peak (101) of Y-doped ZnO was shifted towards lower θ value (Fig. 1b). These observations confirm that although the Y^{3+} dopant seems to have been successfully accommodated into ZnO lattice, the large difference in the ionic radii of Y^{3+} (1.04 Å) and Zn^{2+} (0.74 Å) is likely to interrupt the original atomic arrangement which results in lattice strain.

The obtained XRD patterns of both NPs were subjected to Reitveld analysis using Fullprof software (see Fig. 2a, b) and values of refined cell parameters with profile parameters are listed in Table 1. For Y-doped ZnO, the cell parameter values are large in comparison with those for pure ZnO NPs, which is in agreement with the shift of Bragg peaks towards smaller angle side for doped ZnO. EDS analysis of Y-doped ZnO sample was performed to find its chemical composition

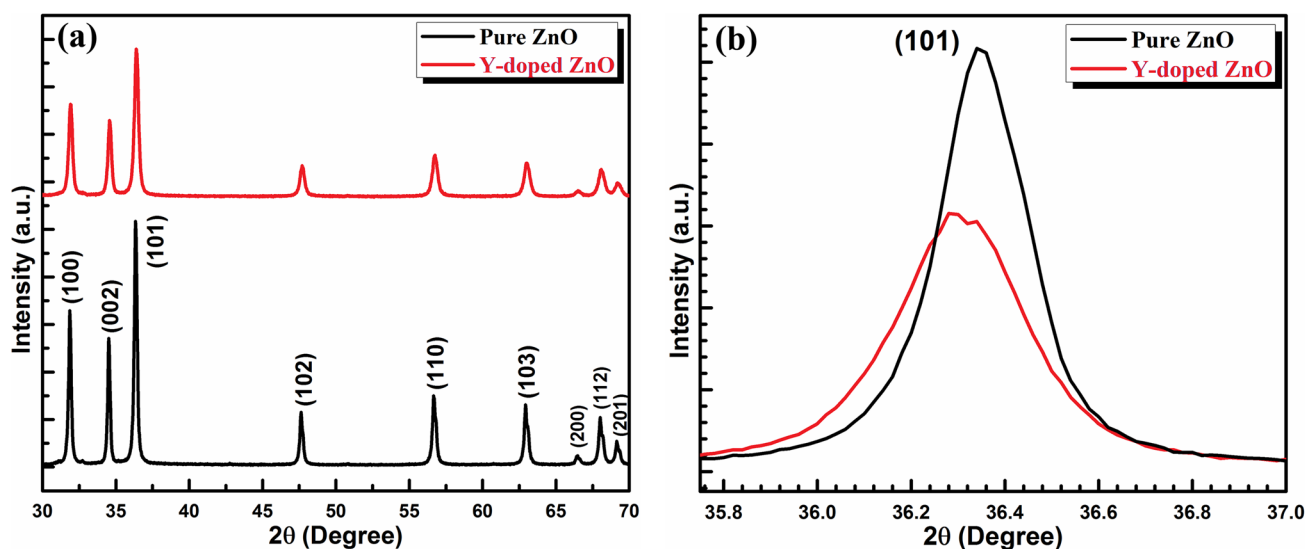


Fig. 1 a XRD patterns of pure and Y-doped ZnO NPs. b The magnified view of most intense (101) Bragg peak

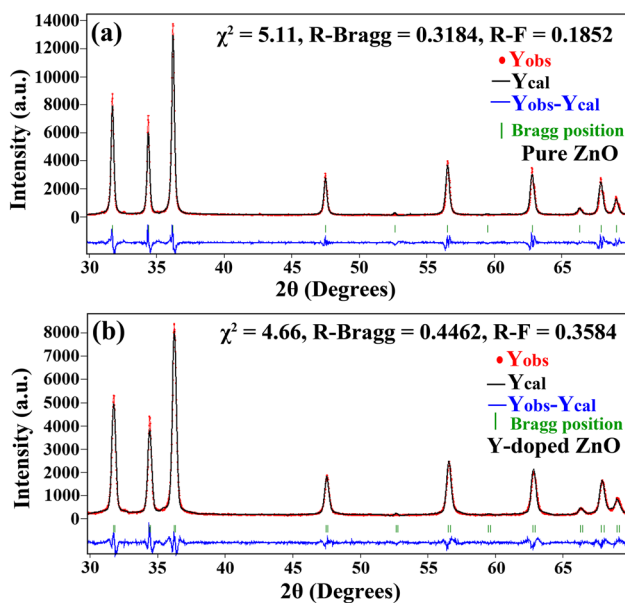


Fig. 2 Rietveld refinement for **a** pure and **b** Y-doped ZnO NPs. The refinement goodness parameter χ^2 was computed to be 5.11 and 4.66 for pure and Y-doped ZnO

Table 1 Rietveld refinement data of pure and Y-doped ZnO nanocrystals

Parameters	Pure ZnO	Y-doped ZnO
Crystal System	Hexagonal	Hexagonal
Cell length, $a=b$ (Å)	3.2538(8)	3.2545(8)
Cell length, c (Å)	5.2114(2)	5.2136(4)
Cell angle $\alpha=\beta$ (°)	90	90
Cell angle γ (°)	120	120
Volume, (Å ³)	47.784(8)	47.825(9)
Rp, Rwp, and χ^2	0.122, 0.139 and 5.11	0.117, 0.135 and 4.66

and is shown in Fig. S1 of Supporting Information file. The EDS spectrum confirms the presence of O, Y, and Zn for Y-doped sample. Thus, both EDS and XRD analysis together indicate the replacement of Zn^{2+} ions by Y^{3+} ions into the ZnO matrix.

3.2 Analysis of crystallite size and strain

In XRD study, an increase in lattice parameters value was noted as a result of Y-doping. This variation in lattice parameters value was accounted to the lattice strain produced by substitution of large Y^{3+} (1.04 Å) dopant ions in place of host Zn^{2+} (0.74 Å) ions. Thus, for a better understanding of the effect of Y^{3+} dopant ions incorporation into the ZnO lattice, it becomes necessary to evaluate the numerical values of crystallite size, lattice strain, deformation stress and deformation energy density for both pure and Y-doped NPs.

3.2.1 Scherrer method

The diffraction peak broadening due to small particle size is given by Scherrer equation as follows [24]:

$$\beta_L = \frac{K\lambda}{L \cos \theta} \quad (1)$$

where, β_L is the broadening (in radians) solely due to small crystallite size, λ is the wavelength of CuK_α radiation (1.54056 Å), L is the crystallite size (in nm), θ is the Bragg peak position and K is the shape factor equal to 0.94. It is noteworthy that β_L in above Eq. (1) is the instrument corrected diffraction peak broadening, which is evaluated as follows,

$$\beta_L = \left[(\beta_o)^2 - (\beta_I)^2 \right]^{1/2} \quad (2)$$

where, β_I is the instrumental broadening (in radians), β_o is the observed diffraction peak broadening. The standard strain free silicon was subjected to XRD under identical conditions on same instrument to determine the instrumental broadening (β_I). The Scherrer equation can be used to evaluate the crystallite size of the ZnO NPs. The Eq. (1) can be reformatted in the logarithmic form as follows:

$$\ln \beta_L = \ln \frac{k\lambda}{L} + \ln \frac{1}{\cos \theta} \quad (3)$$

The plot of $\ln(\beta_L)$ versus $\ln(1/\cos\theta)$ is a straight line with intercept equals to $\ln(k\lambda/L)$ and hence the crystallite size can be evaluated from the intercept $L = \frac{k\lambda}{e^{\text{intercept}}}$. The typical Scherrer equation plots for pure and Y-doped ZnO nanostructures are shown in Figs. 3a and 4a, respectively. The average crystallite sizes of pure and Y-doped ZnO NPs were calculated to be 57.01 and 31.02 nm, respectively, using Scherrer method (Table 2).

3.2.2 Williamson–Hall methods

Generally, the broadening of X-ray diffraction profile is a combination of both lattice strain (ϵ) and crystallite size. Scherrer equation does not consider the lattice strain contribution to line broadening of a Bragg peak. Williamson–Hall (W–H) proposed a method for separating the size and strain broadening components from total broadening. The individual strain-induced (β_S) and small crystallite size-induced (β_L) contributions to the total broadening are expressed as follows [22]:

$$\beta_S = 4\epsilon \tan \theta \quad (4)$$

$$\beta_{hkl} = \beta_L + \beta_S \quad (5)$$

$$\beta_{hkl} = \frac{K\lambda}{L \cos \theta} + 4\epsilon \tan \theta \quad (6)$$

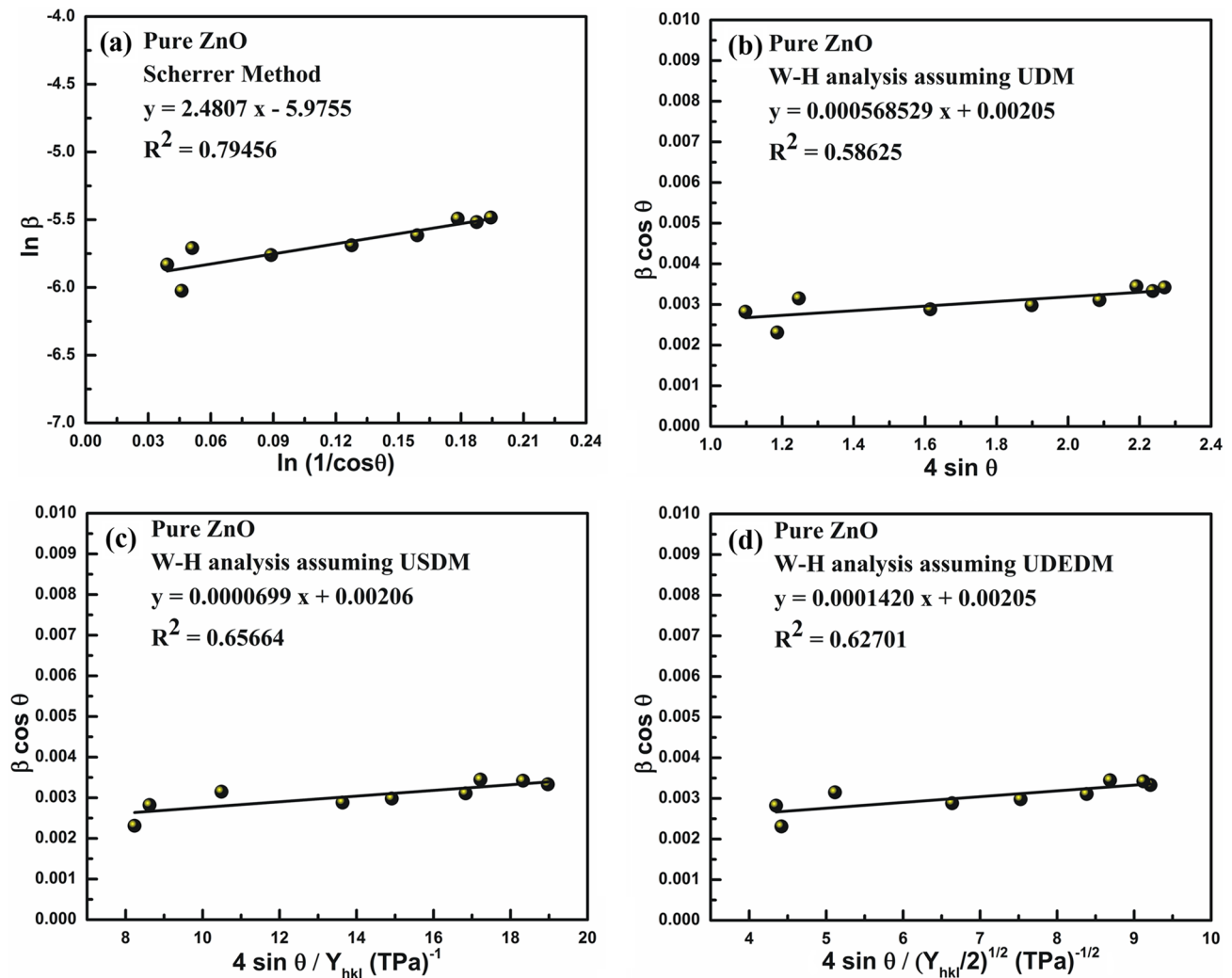


Fig. 3 a Scherrer equation plot for pure ZnO. The W–H analysis assuming **b** UDM, **c** USDM and **d** UDEDM for pure ZnO NPs

where, β_{hkl} is the total integral breadth for (hkl) diffraction peak. Rearranging above Eq. (6) gives:

$$\beta_{hkl} \cos \theta = \frac{K\lambda}{L} + 4\epsilon \sin \theta \quad (7)$$

In above Eq. (7), lattice strain (ϵ) is assumed to be uniform in all crystallographic directions and hence, it is known as uniform deformation model (UDM). Figures 3b and 4b show the plots of $\beta_{hkl} \cos \theta$ versus $4\sin \theta$ for pure and Y-doped ZnO, respectively. The crystallite size was evaluated using the same principles as described above and the lattice strain ($\epsilon = \text{slope}$) was calculated using the slope of the fitted line. The average crystallite size and lattice strain can be

calculated from the y-intercept ($L = \frac{K\lambda}{\text{intercept}}$) and slope ($\epsilon = \text{slope}$) of the fitted line, respectively.

In many cases, it is not correct to assume isotropic nature of lattice strain. Thus, it becomes necessary to consider anisotropic W–H models such as Uniform Stress Deformation Model (USDM) and uniform deformation energy density model (UDEDM). In USDM and according to linear Hooke's law, strain (ϵ) is expressed as a function of stress (σ) and Young's modulus of elasticity (Y_{hkl}): $\epsilon = \sigma/Y_{hkl}$. Thus, after considering this linear stress–strain relationship, the W–H will be modified to the following form:

$$\beta_{hkl} \cos \theta = \frac{K\lambda}{L} + \frac{4\sigma \sin \theta}{Y_{hkl}} \quad (8)$$

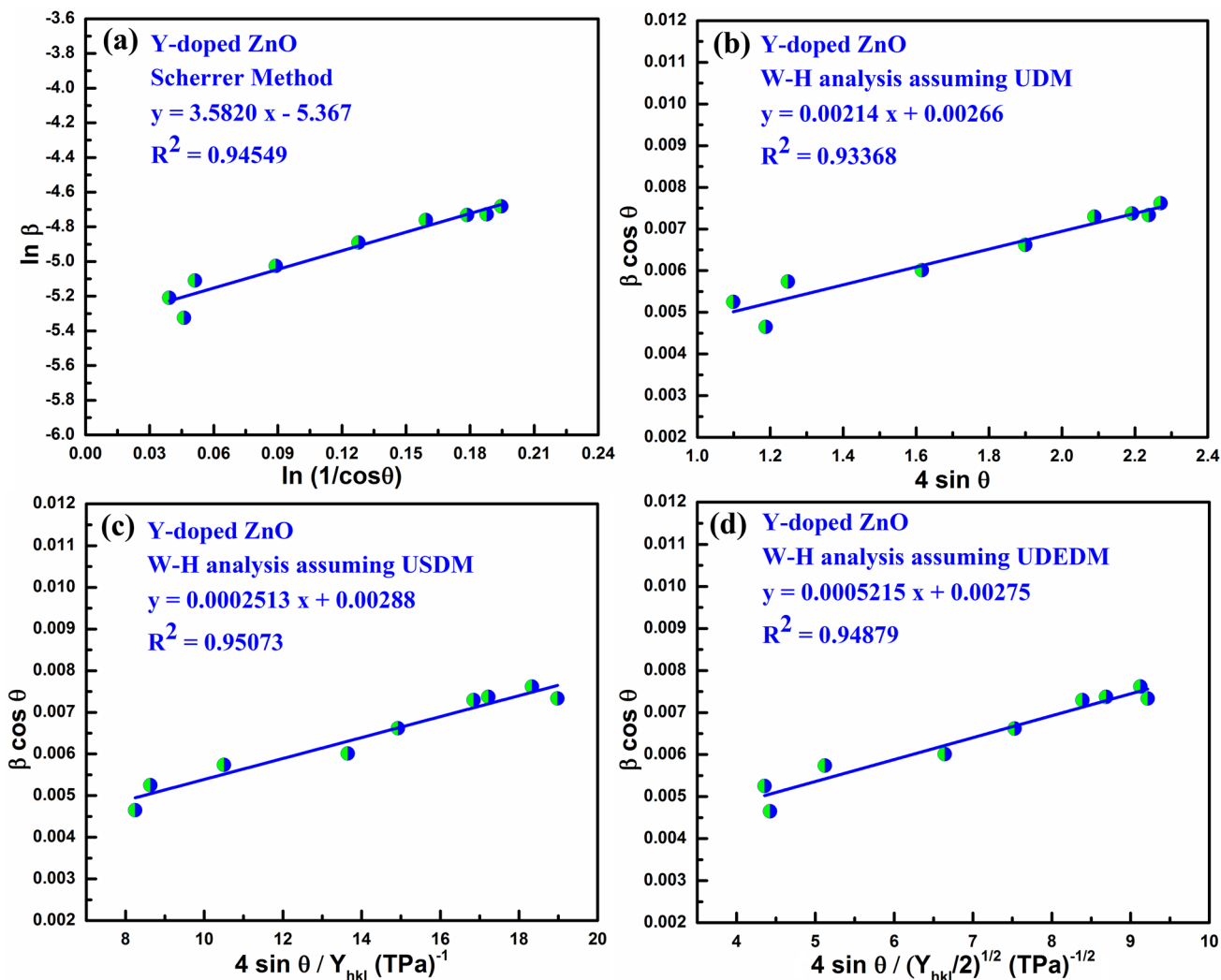


Fig. 4 a Scherrer equation plot for Y-doped ZnO NPs. The W–H analysis assuming b UDM, c USDM and d UEDM for Y-doped ZnO NPs

Table 2 Geometrical parameters of both pure and Y-doped ZnO nanocrystals by Scherrer, W–H and (FESEM and TEM) analysis

Sample	Scherrer method L (nm)	Williamson–Hall method									FESEM and TEM L (nm)
		UDM			USDM			UEDM			
		L (nm)	$\epsilon \times 10^{-3}$	L (nm)	$\epsilon \times 10^{-3}$	σ (MPa)	L (nm)	$\epsilon \times 10^{-3}$	σ (MPa)	u (KJm ⁻³)	
Pure ZnO	57.01	70.64	0.5685	70.30	0.5580	69.95	70.64	0.5669	71.12	20.159	50–240
Y-ZnO	31.02	54.44	2.14	50.28	2.00	251.30	52.66	4.34	543.93	271.96	20–50

$$Y_{hkl} = \frac{\left[h^2 + \frac{(h+2k)^2}{3} + \left(\frac{al}{c} \right)^2 \right]^2}{S_{11} \left(h^2 + \frac{(h+2k)^2}{3} \right)^2 + S_{33} \left(\frac{al}{c} \right)^4 + (2S_{13} + S_{44}) \left(h^2 + \frac{(h+2k)^2}{3} \right) \left(\frac{al}{c} \right)^2} \tag{9}$$

where here a and c are the unit cell parameters for ZnO nanocrystals (see Table 1) and S_{44} , S_{13} , S_{33} and S_{11} are the elastic compliances of ZnO with values of 23.57×10^{-12} , -2.206×10^{-12} , 6.940×10^{-12} and $7.858 \times 10^{-12} \text{ m}^2 \text{ N}^{-1}$, respectively [23]. By plotting $\beta_{hkl} \cos \theta$ as a function of $4 \sin \theta / Y_{hkl}$ (Figs. 3c, 4c), the crystallite size (L) and uniform deformation stress (σ) can be calculated from the extrapolation ($L = K\lambda/\text{intercept}$) and the slope ($\sigma = \text{slope}$) of the fitted line, respectively.

In UDEDM, deformation stress (σ) is anisotropic and energy density (u) is considered to be uniform in all crystallographic directions. The energy density (u) is connected to the strain and Young's modulus by $u = (\epsilon^2 Y_{hkl})/2$. Now the W–H equation can be rewritten as:

$$\beta_{hkl} \cos \theta = \frac{K\lambda}{L} + 4 \sin \theta \left(\frac{2u}{Y_{hkl}} \right)^{1/2} \quad (10)$$

Figures 3d and 4d show the plots of $4 \sin \theta (2/sY_{hkl})^{1/2}$ against $\beta_{hkl} \cos \theta$ for pure and doped ZnO, respectively. Slopes of linear fits give the energy density ($u = (\text{slope})^2$) and y-intercepts of the fitted lines give crystallite size ($L = K\lambda/\text{intercept}$). The geometrical parameters of both pure and Y-doped ZnO NPs obtained using W-H analysis (UDM, USDM & UDEDM models) are summarized in Table 2.

From Table 2, it can be concluded that the crystallite size of ZnO NPs decreased as a result of Y-doping. Also, it can be observed that lattice strain increases as a result of

Y-doping which clearly explains the increase in cell parameter values for doped ZnO NPs.

3.3 Analysis of morphology

In the past two decades, a variety of interesting morphologies of ZnO NPs have been synthesized by various research groups, namely quantum dots [27], nanospheres [28, 29], nanocombs [30], nanobelts [31], nanorods [24], nanoplates [32], polyhedral cages [33] and many more. Controlling the morphology of ZnO nanostructures has gained great attention of many researchers in recent times because of their unique shape-dependent characteristics. ZnO structures at the nanoscale demand different external shapes with varying surface area for utilizing their novel size effects in improving the efficiencies of many practical applications. Towards this aim, the morphologies of pure ZnO and Y-doped ZnO NPs were carefully investigated with FESEM and TEM techniques.

Figure 5 shows the typical FESEM and TEM images of the pure ZnO NPs. The pencil like morphology of pure ZnO NPs is very much evident from their FESEM and TEM images (see Fig. 5a–c). The nanopencils (NPCs) have diameters in the range of 50–240 nm and length of about 0.4–1.0 μm . Figure 5d depicts the corresponding SAED (selected area electron diffraction) pattern obtained from the pure ZnO NPCs. SAED pattern clearly depicts the single crystalline nature of synthesized NPCs with the hexagonal wurtzite structure, which is in consistency with the powder XRD results (see Sect. 3.1).

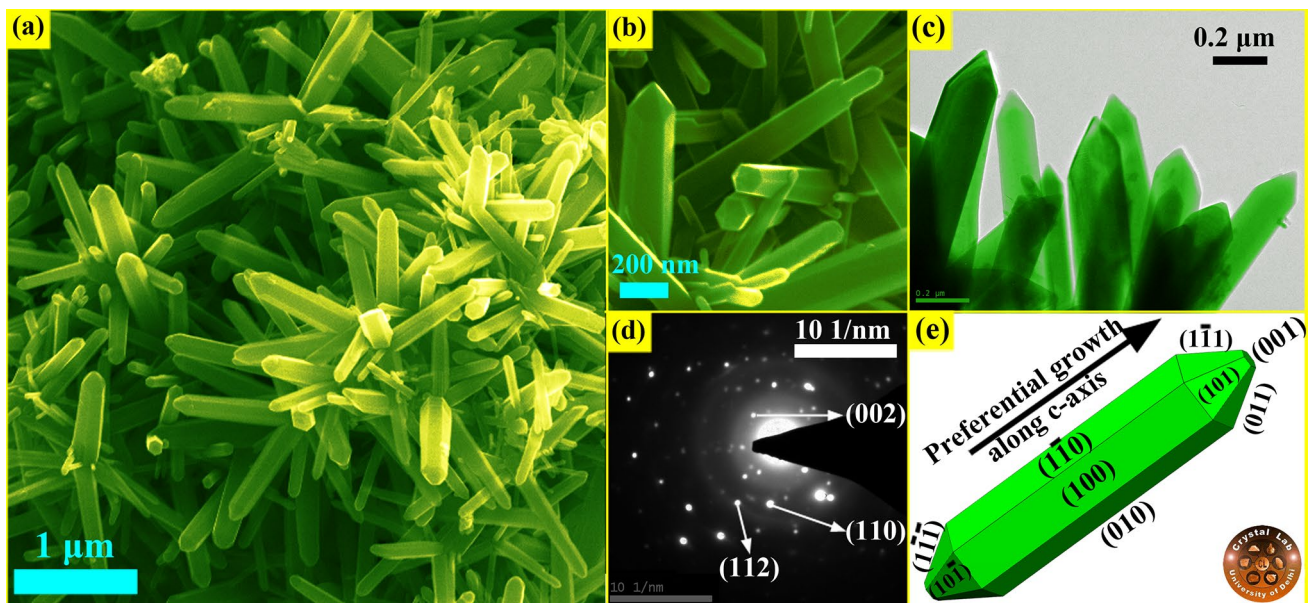


Fig. 5 a, b FESEM images of ZnO nanopencils. It can clearly be observed that the pure ZnO crystals are formed in the shape of rods with hexagonal cross-section and pencil like tip (diameter

~50–240 nm and length ~0.4–1.0 μm). c TEM image and d SAED pattern of pure ZnO pencils. e Indexed morphology of a ZnO pencil

Figure 5e depicts the indexed morphology of ZnO pencils. The unique formation of pencil-like shape of ZnO NPs can be understood on the basis of energies and relative growth velocities of various facets appearing in its morphology. Structurally, ZnO NPCs consist of twenty planes out of which six symmetric $\{10\bar{1}0\}$ planes are non-polar and fourteen planes ($\{01\bar{1}1\}$, $\{01\bar{1}\bar{1}\}$, (0001) and (000 $\bar{1}$)) are polar in nature. Top (001) and bottom (00 $\bar{1}$) facets of ZnO crystal are known as chemically active Zn terminated and chemically inert O-terminated planes, respectively [26]. The ideal growth velocities (rates) of various planes for the case of ZnO crystal can be listed as: (0001) > $\{01\bar{1}1\}$ > $\{10\bar{1}0\}$ > $\{01\bar{1}\bar{1}\}$ > (000 $\bar{1}$). The (0001) is fastest growing plane as it has higher surface energy and thus, it is least visible in the final shape of ZnO NPCs.

As shown in Fig. 6a, Y-doped ZnO NPs consists of 3D flower-like architectures assembled by 2D nanosheets (building blocks). These 3D Y-doped ZnO flowers have diameters in the range of 1.0–3.0 μm and are made up of interconnected Y-ZnO nanosheets (NSs) with a thickness of about 25–50 nm. The enlarged views of interconnected Y-ZnO NSs are depicted in Fig. 6b, c. The morphology of the Y-ZnO NSs was further investigated in detail using TEM analysis. Figure 6d shows the typical TEM image of one Y-ZnO NS. A large quantity of nanosized pores with sizes of 2–20 nm in diameter can be observed on the surface of NS,

which confirms the porous structure of as-obtained Y-doped ZnO sheets. The SAED pattern corresponding to the porous Y-ZnO NS as shown in Fig. 6e consists of well ordered dots indicating the single crystalline nature of these sheets. The presence of (001) and (004) diffraction peaks (in SAED pattern) confirms the fact that the most visible plane (i.e., the top plane) in the morphology of Y-ZnO NS is (001) plane.

As discussed in our previous manuscript on 2D Y-ZnO sheets [26], the introduction of Y^{3+} ions into growth solution leads to the formation of YO_2^- dopant anionic units. These YO_2^- anionic units attach themselves to the Zn-polarized plane of ZnO to inhibit its growth along 'c' crystallographic direction. This effective growth of the crystal nuclei along the lateral directions (perpendicular to $\{10\bar{1}0\}$ planes) leads to the formation of 2D Y-doped ZnO nanosheets.

This drastic transition in the morphology of ZnO crystal from 1D nanopencils (pure ZnO) to 2D nanosheets (for Y-ZnO) has proven to be beneficial in boosting up the piezo-conversion efficiency of ZnO from 12 to 420 pm/V for 2D Y-ZnO NSs [26]. Moreover, Y-doped ZnO porous NSs with a large polar surface area ((001) plane) is expected to exhibit many novel characteristics over 1D pure ZnO NPCs. In this paper, we will focus on dielectric and ferroelectric properties of 2D Y-doped ZnO NSs.

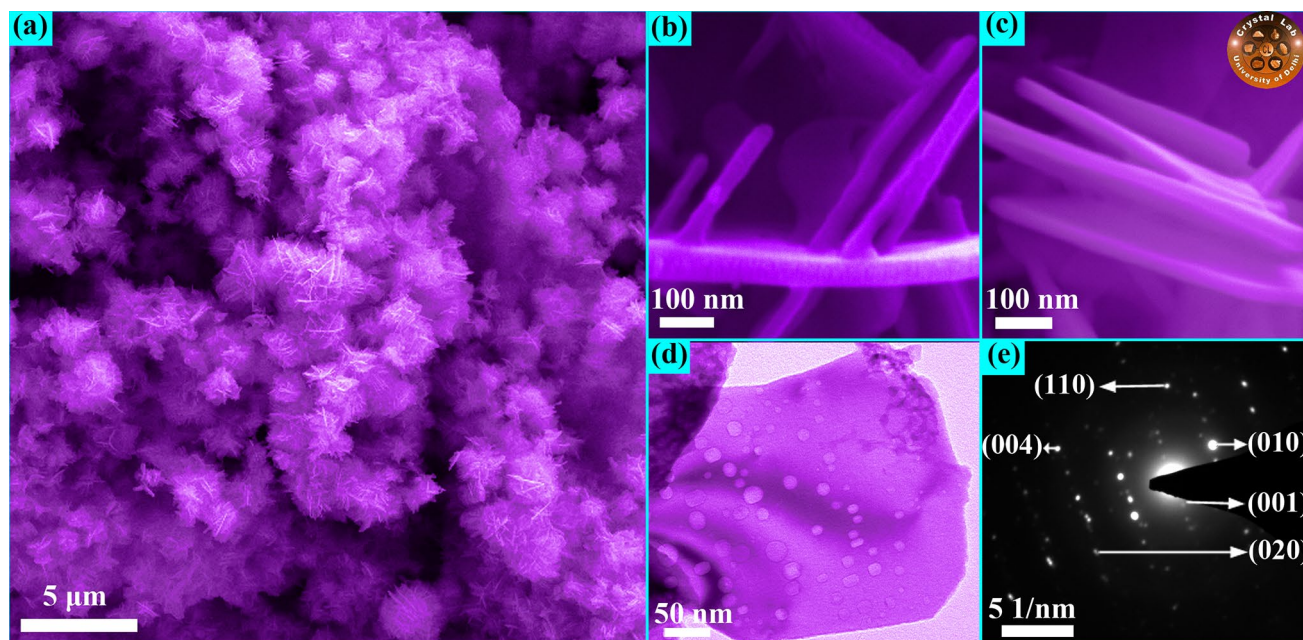


Fig. 6 **a** FESEM image overview of 3D flower-like Y-ZnO architectures assembled by 2D nanosheets of thickness 25–50 nm. **b** and **c** Enlarged views of interconnected Y-ZnO NSs. **d** TEM image of a

single Y-ZnO porous sheet with nanopores of diameters 2–25 nm. **e** Indexed SAED pattern of Y-ZnO porous sheet

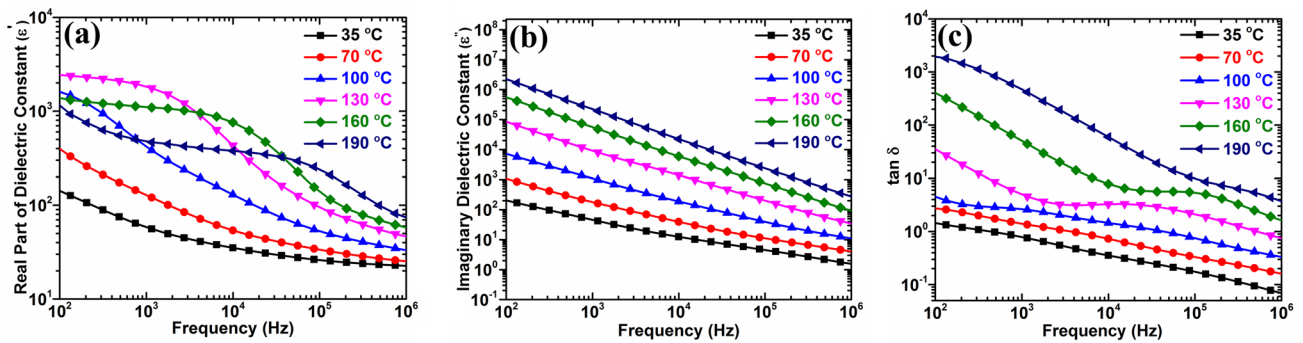


Fig. 7 Variation of **a** the real component of the permittivity (ϵ'), **b** the imaginary component (ϵ'') of the permittivity, and **c** dielectric loss with frequency for Y-doped ZnO NSs measured at different applied temperatures

3.4 Dielectric study

3.4.1 Permittivity and loss studies

Dielectric permittivity of a material is a dimensionless complex number in a sense that the real component (ϵ') quantifies the stored energy or polarizability in a dielectric under an applied electric field, whereas the imaginary part (ϵ'') accounts for the dissipated energy. Both real (ϵ') and imaginary (ϵ'') components are the functions of frequency of continuously changing electric field as shown in Fig. 7a, b, respectively. The value of real dielectric constant for Y-ZnO NSs was found to decrease with increasing frequency at all the temperatures. Furthermore, a plateau region (frequency independent response) starts to appear at higher temperatures, which indicates a shift in the relaxation peak with respect to temperature. Another measure of dissipated energy is dielectric loss ($\tan \delta$), which can be derived from fundamental dielectric parameters (ϵ' and ϵ'') and is defined as the ratio (ϵ''/ϵ'). Figure 7c depicts the variation of dielectric loss ($\tan \delta$) with frequency (from 100 Hz to 1 MHz) at different applied temperatures. For the spectrums recorded at lower temperatures (see curves at 35 and 70 °C), the dielectric loss goes on decreasing with increase in frequency. Whereas, for the dielectric loss spectrums recorded at higher temperatures (see curves at 100, 130, 160 and 190 °C), the dielectric loss first decreases with frequency and then shows a little hump at certain frequency which shifts towards higher frequency with increase in temperature. This hump observed for frequency dependence curve of dielectric loss (at higher temperature) confirms the relaxation process and is in consistency with the plateau region obtained for the frequency dependence curve of real part of dielectric constant (see Fig. 7a).

The major contribution to dielectric polarization of a nanomaterial comes from orientational polarization and space charge polarization. The large values of dielectric constant ($\epsilon' \sim 126$ @ 35 °C, 100 Hz) and dielectric loss

($\tan \delta \sim 1.44$ @ 35 °C, 100 Hz) in low frequency region can be attributed to the dominant nature of space charge polarization in ZnO nanostructures at lower frequencies. It is a well known fact that ZnO NPs exhibit space charge polarization due to large amount of defects, such as micro-pores at the grain boundaries and various surface defects such as dangling bonds and vacancy cluster. These surface defects can cause a change of negative and positive space charge distributions at the interfaces. Positive and negative space charge distribution at the interfaces move towards negative and positive poles of the applied electric field, respectively. Now, these moving space charges get trapped by the defects leading to formation of dipoles and hence, non-zero space charge polarization. Nevertheless, at higher frequencies, dielectric response of space charges cannot keep up with the fast variation of applied electric field, resulting in the reduction of dielectric constant and dielectric loss of ZnO NPs. Moreover, it is noteworthy that orientational polarization originates as a result of rotational displacement of dipoles in the ZnO nanostructure and is the dominant source of non-zero dielectric polarization in high frequency region. The possible source of orientational polarization in ZnO nanostructure is the existence of large amount of oxygen vacancies and zinc interstitials. Under the application of an external electric field, the oxygen (O^{2-}) vacancies and the Zn^{2+} ions in the neighborhood gives rise to a large amount of dipole moments. These dipole moments will try to align along the direction of the external electric field, which results in orientational polarization in ZnO nanostructure. Furthermore, on further increasing the frequency of applied external field, frequency independent responses for dielectric constant are observed ($\epsilon' \sim 23$ @ 35 °C, 1 MHz). The low value of dielectric loss at higher frequency ($\tan \delta \sim 0.05$ @ 35 °C, 1 MHz) of the Y-ZnO NSs makes it a potential futuristic material for high frequency applications.

The variation of real (ϵ') component of dielectric constant, imaginary (ϵ'') component of dielectric constant and dielectric loss ($\tan \delta$) with temperature (35–200 °C) at selected

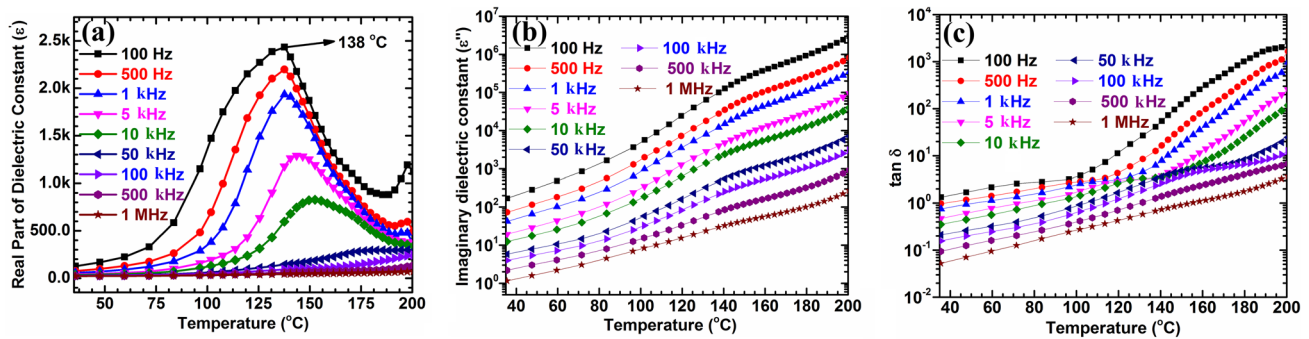


Fig. 8 Temperature dependence of **a** the real component of the permittivity (ϵ'), **b** the imaginary component (ϵ'') of the permittivity and **c** dielectric loss of Y-doped ZnO NSs measured at different applied frequencies. Ferroelectric to paraelectric phase transition at $T_c = 138^\circ\text{C}$

frequencies (100 Hz to 1 MHz) are displayed in Fig. 8a, b, c, respectively. From Fig. 8 it can be clearly observed that Y-doped ZnO NSs exhibit dielectric dispersion, where the dielectric constant decreases with an increase in the frequency of applied electric field. The value of real component of dielectric constant (ϵ') for Y-ZnO NSs (@R.T. & @100 Hz) was found to be 126. Moreover, the dielectric constant (ϵ') increases with an increase in temperature and attains a maxima ($\epsilon'_m \sim 2430$) at transition temperature ($T_c \sim 138^\circ\text{C}$) and thereafter decreases with further increase in applied temperature. Below transition point T_c , the increase in real (ϵ') component of dielectric constant with temperature is attributed to the fact that the dipolar molecules present in Y-ZnO sample are relatively free at higher temperatures and thus, are more susceptible to applied electric field resulting in an increase in polarization. After transition point T_c , decrease in the value of real (ϵ') component of dielectric constant with temperature can be understood as ferroelectric to paraelectric structural phase transition. Moreover, the peak value of dielectric constant (ferroelectric to paraelectric phase transition) shifts towards higher temperatures with an increase in frequency. This mimics relaxor characteristics of Y-ZnO sample and is due to the disability of charge carriers to align too fast with the changing electric field at higher frequencies. Thus, to align all the charge carriers and to restore complete polarization, higher temperature is needed.

Both imaginary (ϵ'') and dielectric loss measure the amount of energy dissipated in the system. Figure 8b, c show the temperature variation of imaginary (ϵ'') and dielectric loss, respectively measured at selected frequencies (100 Hz to 1 MHz). At low temperature, the loss increases at a smaller rate with increase in temperature but at higher temperature it shows a significant increase with increasing temperature, which is commonly observed phenomenon for most of the ceramic materials due to space charge polarization [34]. Additionally, large value of dielectric loss observed at higher temperature may be attributed to macroscopic distortion of charges [34]. The trend shown by Y-ZnO

Table 3 A brief comparison of transition temperature (T_c) of Y-ZnO NSs with that of earlier reported values for various other doped-ZnO samples

S.No.	Doped ZnO sample	T_c ($^\circ\text{C}$)	References
1	Li-doped ZnO thin films	57	[16]
2	Li/Mg co-doped ZnO thin films	87	[17]
3	Mg-doped ZnO films	110	[38]
4	Cr-doped ZnO thin films	95	[21]
5	Ba doped ZnO nanoparticles	330	[20]
6	V-doped ZnO nanorods	345	[39]
7	Ce ³⁺ doped ZnO nanorods	48	[25]
8	Eu ³⁺ doped ZnO nanorods	230	[22]
9	La ³⁺ doped ZnO nanorods	276	[24]
10	Gd ³⁺ doped ZnO nanorods	215	[23]
11	Y ³⁺ doped ZnO nanosheets	138	[Present Work]

NSs is a common trend where dielectric loss increases with temperature and decreases with frequency [35].

Pure ZnO is well known to be ferroelectrically in-active and does not show any ferroelectric to paraelectric transition in temperature dependence curve of dielectric constant [36]. Here, it can be considered that the substitution of host Zn²⁺ ions by dopant Y³⁺ ions induces structural changes in host ZnO lattice, which plays an important role in introducing ferroelectric phase in Y-ZnO NSs. This ferroelectric to paraelectric phase transition at 138°C in Y-doped ZnO NSs arises as a result of order–disorder feature of off-centered substitutional Y³⁺ ions as well as due to the displacive feature of relative translational shifts in Zn and O sublattices [37]. This dielectric anomaly observed for Y-doped ZnO NSs is similar to previously reported results for Li-doped ZnO ceramics, (Mn, Li) co-doped ZnO NRs, Eu-doped ZnO NRs, La-doped ZnO NRs and Gd-doped ZnO NRs, which are summarized in Table 3. Finally, it can be concluded that the high value of dielectric constant (ϵ') and transition temperature (T_c) found in Y³⁺-doped ZnO samples may be

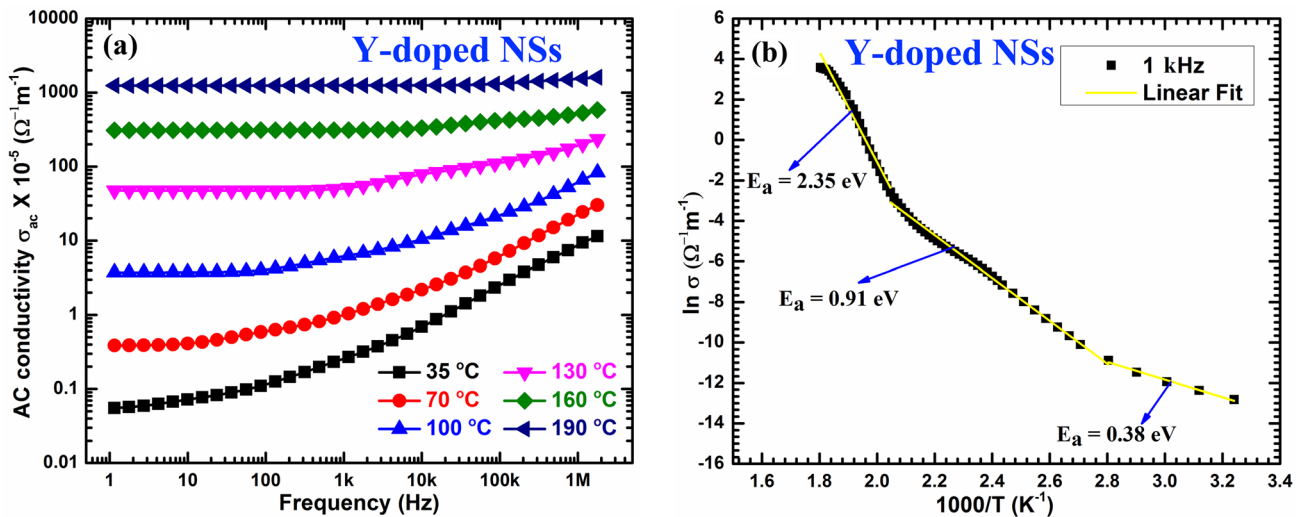


Fig. 9 a The frequency dependence of AC conductivity of Y-doped ZnO NSs. b Plot of $\ln(\sigma_{ac})$ against $1000/T$ (@ 1 kHz) for Y-doped ZnO NSs

beneficial from application point of view specially for wide-temperature range ferroelectrics and charge storage devices.

3.4.2 AC conductivity analysis

Figure 9a displays the logarithmic plot of frequency dependent AC conductivity (σ_{ac}) of Y-doped ZnO NSs. It is obvious from the curve that the value of conductivity (σ_{ac}) progressively increases with increase in frequency of applied alternating electric field. This is because with increase in frequency there would be an enhancement in hopping frequency of electron and hence, migration of electron would be faster. σ_{ac} was evaluated from the dielectric loss data using this relation, $\sigma_{ac} = 2\pi f \tan\delta \epsilon' \epsilon_0$, here $\tan \delta$ denotes the dielectric loss, f is the frequency of the applied field, ϵ_0 is free space permittivity and ϵ' is the real part of dielectric constant. The conductivity curves at all temperatures show that the conductivity of the titled sample is frequency independent in the low frequency regime and this frequency independent region increases with increase in temperature. Conversely, in high frequency regime, the value of conductivity increases rapidly with increase in frequency which may be attributed to little Polaron jumping [40]. The frequency independent conductivity is due to significant contribution from the dc conductivity. In higher frequency regime, the contribution from ac conductivity starts to dominate. This can be easily understood by Jonscher power law, $\sigma = A\omega^s$, where A denotes a constant, ω is the angular frequency of applied electric field and exponent 's' is a frequency dependent parameter [41]. Similar type of AC conductivity behavior has been observed for various other doped ZnO samples, namely Al-doped ZnO, (Al, Ni) co-doped ZnO [42], Ag-doped ZnO [43] and Gd-doped ZnO NPs [23], etc.

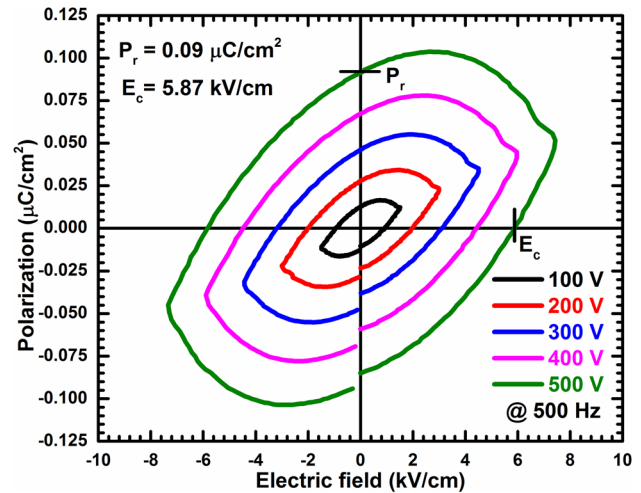


Fig. 10 Hysteresis loops of Y-doped ZnO NSs

The Arrhenius equation was employed to evaluate the activation energy of the Y-doped ZnO NSs and is expressed as: $\sigma_{ac} = \sigma_0 \exp(-E_a/k_B T)$, here, σ_0 denotes the pre-exponential factor and k_B denotes the Boltzmann constant. Figure 9b depicts the curve of $\ln \sigma_{ac}$ plotted against $1000/k_B T$ (@ 1 kHz). The values of activation energies in Y-ZnO NSs were computed to be 2.35, 0.91 and 0.38 eV at various temperature range.

Table 4 Comparison of ferroelectric parameters (P_r and E_c) of Y-doped ZnO nanosheets and various other doped ZnO samples

S.No.	ZnO sample	E_c (kV/cm)	P_r ($\mu\text{C}/\text{cm}^2$)	References
1	Ba doped ZnO nanoparticles	2.02	1.01	[20]
2	Cr^{3+} doped ZnO films	50	0.2	[19]
3	Cr-doped ZnO nanorods	0.96	6.18	[44]
4	Mg-doped ZnO films	8	0.2	[38]
5	V-doped ZnO ceramics	0.45	2.0	[45]
6	Eu-doped ZnO nanorods	5.81	0.11	[22]
7	La-doped ZnO nanorods	1.33	0.027	[24]
8	Gd-doped ZnO nanorods	16.41	0.29	[23]
9	Y-doped ZnO nanosheets	5.87	0.09	[Present Work]

3.5 Ferroelectric study

3.5.1 Polarization hysteresis behavior

Figure 10 presents the room temperature P-E hysteresis loops of the studied Y-doped ZnO NPs registered at different voltages (@ 500 Hz). It is evident in Fig. 10 that Y-doped ZnO sample is a weak ferroelectric material with a remnant polarization (P_r) of $0.09 \mu\text{C}/\text{cm}^2$ and a coercive field (E_c) of 5.87 kV/cm at 500 V. Table 4 summarizes a brief comparison of ferroelectric parameters (P_r and E_c) of earlier reported doped ZnO nanostructures. In Y-doped ZnO NPs, there is a mismatch in the ionic radii of impurity (Y^{3+} ; 1.04 \AA) and host (Zn^{2+} ; 0.74 \AA) ions. Due to this ionic radii mismatch, impurity (Y^{3+}) ions can occupy off-centered and interstitial positions, thereby forming permanent dipole moments locally that can introduce the ferroelectric characteristics. Similar reports on origin of ferroelectricity from ionic radii difference are available in literature [19–24, 38, 44, 45]. In our previous study on Y-doped ZnO NSs [26], we have proposed that the ratio of (ionic charge)/(ionic size) of the dopant ion plays a vital role in deciding the electromechanical response of doped ZnO. The $\left(\frac{\text{ionic charge}}{\text{ionic size}}\right)$ ratio of dopant Y^{3+} ion is 2.88, which is greater than that for host Zn^{2+} ion (2.70) [26]. Due to this difference in the value of $\left(\frac{\text{ionic charge}}{\text{ionic size}}\right)$ ratio, the non-collinear Y-O bonds hold stronger polarity than that of Zn-O bonds, which makes the flipping of these locally formed permanent dipole moments much easier and hence originates ferroelectricity in ZnO. The non-zero remnant polarization obtained for Y-ZnO sample makes it a futuristic material of choice for designing memory component of nonvolatile ferroelectric random access memory.

3.5.2 Time-dependent leakage analysis

From the P-E hysteresis loops, one can see that Y-doped ZnO nanocrystals display lossy ferroelectric character. In order to determine the nature of the leakage present in the

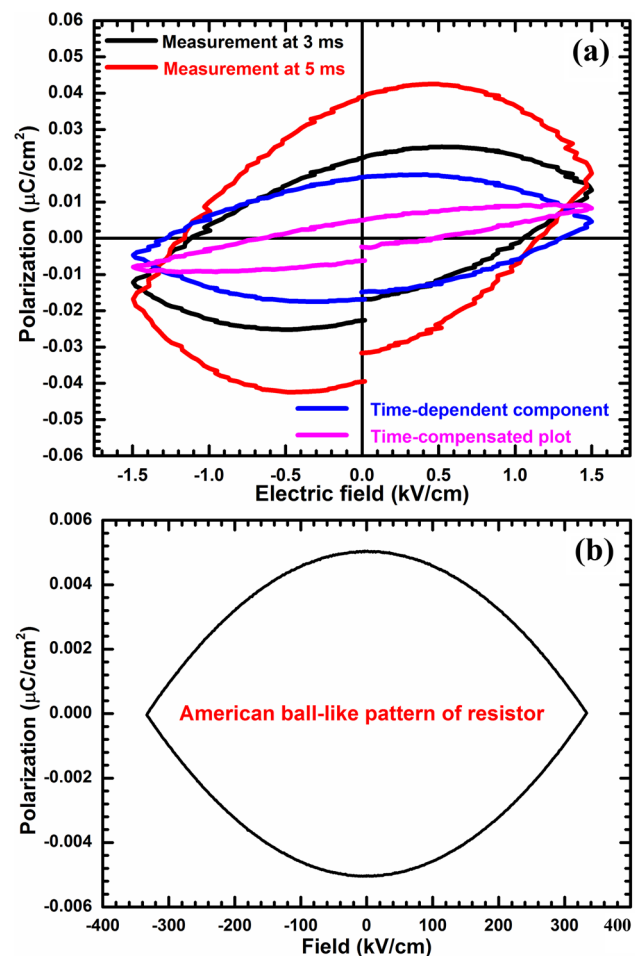


Fig. 11 a TDC plots revealing resistive leakage in Y-ZnO NSs sample. b The hysteresis curve of a pure resistor

sample, time-dependent compensated (TDC) hysteresis measurements were performed on it. In this technique, two hysteresis loops were traced for Y-ZnO NSs at different frequencies (2 and 4 ms), which are shown by black and red curves, respectively, in Fig. 11a. From these two hysteresis loops, the time independent and time-dependent

features were separated by using the Meyer et al. algorithm [46–48]. Now, one of the hysteresis plots is compensated by this time-dependent component to get leakage compensated hysteresis trace (shown using pink trace in Fig. 11a). It is noteworthy that the resistive leakage is a frequency dependent parameter. Hence, by compensating the hysteresis loop with the time-dependent component, we are able to eliminate the contribution due to resistive leakage. The shape of the time-dependent component curve (shown in blue curve in Fig. 11a) for Y-ZnO NSs matches well with the hysteresis curve of a pure resistor (see Fig. 11b), which confirms the presence of resistive leakage in Y-ZnO sample. This explains the unsaturated nature of P-E hysteresis loops. In addition to dielectric phase transition and P-E hysteresis studies, these results prove well that Y-ZnO NSs present a ferroelectric (though weak) character.

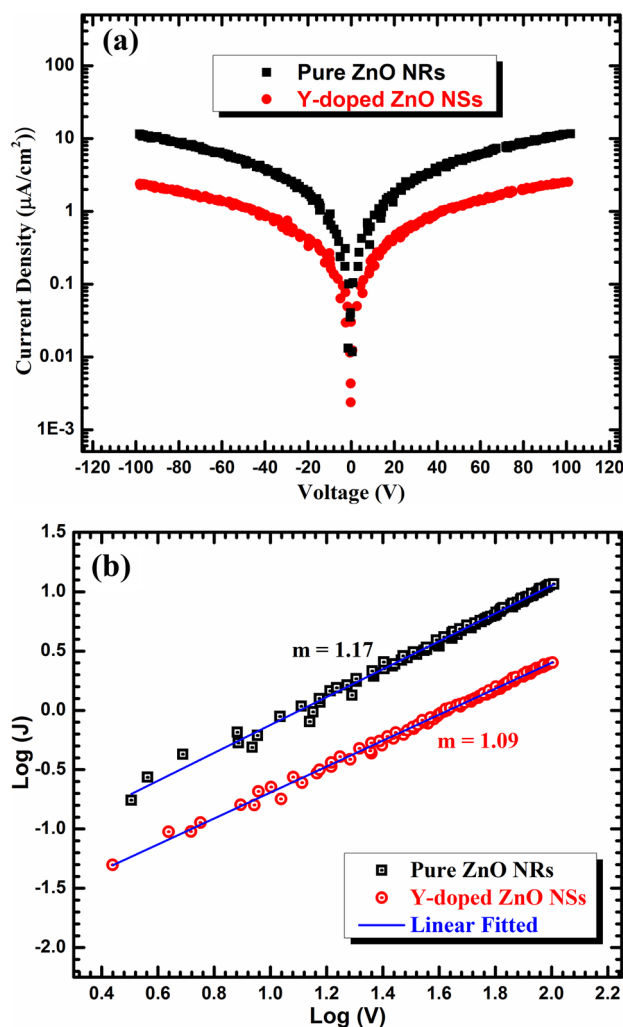


Fig. 12 **a** J–V plots for pure ZnO NPCss and Y-doped ZnO NSs recorded at room temperature. **b** Log (J) versus Log (V) characteristics of pure ZnO NPCs and Y-doped ZnO NSs

In order to quantify the resistive leakage present in titled ZnO sample, J–V characteristics curve was recorded in the following section.

3.6 J–V Characteristics

The study of conduction mechanism helps us to gain better understanding of the ferroelectric characteristics of a material [49]. J–V characteristics of both the pure ZnO NPCs and Y-doped ZnO NSs were traced on the silver coated ZnO pellets, which serves as a metal-semiconductor-metal (M-S-M) junction. Figure 12a displays the semi-log plot of leakage current density (J) against applied electric field (E) for both ZnO samples. The symmetric nature of leakage current density about the ordinate (J-axis) confirmed the ohmic characteristics of M-S junctions for both the pellets [23]. Figure 12b presents the plot of log J against log V. The behavior of these curves presented in Fig. 12b is governed by the power law: $J \propto E^m$, here m (slope) conveys the nature of conduction mechanism [23]. The values of slope (m) were measured to be 1.17 for pure ZnO NPCs and 1.09 for Y-doped ZnO NSs, which can be analyzed on the basis of ohmic conduction and space-charge limited conduction (SCLC) mechanisms [23]. The leakage current got decreased as a result of Y-doping in ZnO NPs. Also, the dc conductivity was observed to decrease as a result of Y-doping, which was measured to be 5.7×10^{-9} mho cm^{-1} for pure ZnO NPCs and 1.7×10^{-9} mho cm^{-1} for Y-doped ZnO NSs. This reduced leakage current density for Y-ZnO NSs may be due to an increase in Schottky barrier height by Y-doping, which makes it a futuristic material for ferroelectric capacitor.

4 Conclusions

The above presented experimental results and discussions on Y-doped ZnO nanosheets can be summarized as follows:

1. Pure and Y-doped ZnO NPs were easily synthesized by wet chemical co-precipitation route.
2. By doping ZnO with yttrium, the cell parameter values got increased and the Bragg peaks got shifted towards smaller angle. Moreover, hexagonal wurtzite crystal-line phase was observed for both pure and doped nano-structures.
3. Dopant Y^{3+} ions played an inevitable role in deciding the final external shape of ZnO nanocrystals. A drastic change in the morphology of ZnO nanocrystals from 1D NPCs (diameter ~ 50 – 240 nm) to 2D NSs (thickness ~ 25 – 50 nm) was observed as a result of Y-doping.
4. By addition of Y^{3+} ions as dopant cations, the growth habit of pure ZnO crystal got greatly influenced and the relative growth velocity of each crystal plane got

changed, which led to formation of 2D sheet like network.

5. TEM analysis further confirmed the porous nature of Y-doped ZnO NSs with nanosized pores of diameter ~2–20 nm.
6. From Scherrer and W-H methods, it can be concluded that the crystallite size decreased from 70 to 53 nm and lattice strain increased from 0.57×10^{-3} to 4.34×10^{-3} as a result of Y-doping.
7. A higher dielectric constant ($\epsilon' \sim 126$ @ 35 °C, 100 Hz) and large ferroelectric to paraelectric phase transition at 138 °C were observed for Y-doped ZnO NSs.
8. The most significant change which Y^{3+} substitution brings is the appearance of switchable polarization i.e., ferroelectricity in ZnO. The remnant polarization (P_r) and coercive field (E_c) were found to be $0.09 \mu\text{C}/\text{cm}^2$ and 5.87 kV/cm, respectively.
9. Time-dependent compensated (TDC) hysteresis measurements confirmed the presence of resistive leakage in Y-ZnO sample.
10. The leakage current got decreased on Y-doping. The dc conductivity was found to decrease from 5.7×10^{-9} to 1.7×10^{-9} mho cm^{-1} as a result of Y-doping in ZnO nanocrystals.

Finally, we conclude that high value of dielectric constant ($\epsilon' \sim 126$ @ 35 °C, 100 Hz) and high temperature ferroelectricity ($P_r \sim 0.09 \mu\text{C}/\text{cm}^2$, $E_c \sim 5.87$ kV/cm & $T_c \sim 138$ °C) adds another dimension to the multifunctional characteristics ($d_{33} \sim 420$ pC/N) of Y-doped ZnO nanosheets and make it a futuristic candidate for nanoscale charge storage and memory devices.

Acknowledgements The authors are grateful to the ARMREB, DRDO (Sanction No.: ARMREB/MAA/2015/163), India, and the Department of Science and Technology (Sanction No.: EMR/2015/000385), India for providing financial support. N.S. expresses her warm thanks to the Principal, SGTB Khalsa College, for encouraging her to do research work. S.G. and A.J.J. are thankful to CSIR and DRDO, respectively, for Senior Research Fellowship.

References

1. H. Bilz, A. Bussmann-Holder, W. Jantsch, P. Vogl, *Dynamical Properties of IV–VI Compounds* (Springer-Verlag, Berlin, 1983)
2. S. Katayama, K. Murase, *Solid State Commun.* **36**, 707 (1980)
3. P.B. Littlewood, *J. Phys. C Solid State Phys.* **12**, 4459 (1979)
4. A. Marbeuf, C. Mondoloni, R. Triboulet, J. Rioux, *Solid State Commun.* **75**, 275 (1990)
5. E. Fredj, R. Weil, E. Muranevich, L. Benguigui, *Ferroelectrics* **125**, 57 (1992)
6. A. Onodera, N. Tamaki, Y. Kawamura, T. Sawada, H. Yamashita, *Jpn. J. Appl. Phys.* **35**, 5160 (1996)
7. J.C. Phillips, *Bonds and Bands in Semiconductors* (Academic Press, London and New York, 1973)
8. G. Heiland, E. Mollwo, F. Stöckmann, *Solid State Phys.* **8**, 191 (1959)
9. C. Campbell, *Surface Acoustic Wave Devices and Their Signal Processing Applications* (Academic Press, San Diego, 1989)
10. L. Zhu, W. Zeng, *Sensors Actuators A Phys.* **267**, 242 (2017)
11. R. Kumar, O. Al-Dossary, G. Kumar, A. Umar, *Nano-Micro Lett.* **7**, 97 (2015)
12. Z.L. Wang, *Science* **312**, 242 (2006)
13. D. Kim, K.Y. Lee, M.K. Gupta, S. Majumder, S.-W. Kim, *Adv. Funct. Mater.* **24**, 6949 (2014)
14. K.Y. Lee, J. Bae, S. Kim, J.-H. Lee, G.C. Yoon, M.K. Gupta, S. Kim, H. Kim, J. Park, S.-W. Kim, *Nano Energy* **8**, 165 (2014)
15. M.K. Gupta, J.-H. Lee, K.Y. Lee, S.-W. Kim, *ACS Nano* **7**, 8932 (2013)
16. A. Onodera, N. Tamaki, K. Jin, H. Yamashita, *Jpn. J. Appl. Phys.* **36**, 6008 (1997)
17. A. Onodera, K. Yoshio, H. Satoh, H. Yamashita, N. Sakagami, *Jpn. J. Appl. Phys.* **37**, 5315 (1998)
18. T. Nagata, T. Shimura, Y. Nakano, A. Ashida, N. Fujimura, T. Ito, *Jpn. J. Appl. Phys.* **40**, 5615 (2001)
19. Y.C. Yang, C. Song, X.H. Wang, F. Zeng, F. Pan, *J. Appl. Phys.* **103**, 74107 (2008)
20. G. Srinet, R. Kumar, V. Sajal, *Mater. Lett.* **126**, 274 (2014)
21. Y.C. Yang, C.F. Zhong, X.H. Wang, B. He, S.Q. Wei, F. Zeng, F. Pan, *J. Appl. Phys.* **104**, 64102 (2008)
22. H. Yadav, N. Sinha, S. Goel, B. Kumar, *J. Alloys Compd.* **689**, 333 (2016)
23. S. Goel, N. Sinha, H. Yadav, S. Godara, A.J. Joseph, B. Kumar, *Mater. Chem. Phys.* **202**, 56 (2017)
24. S. Goel, N. Sinha, H. Yadav, A.J. Joseph, B. Kumar, *Phys. E Low-Dimensional Syst. Nanostructures* **91**, 72 (2017)
25. N. Sinha, G. Ray, S. Bhandari, S. Godara, B. Kumar, *Ceram. Int.* **40**, 12337 (2014)
26. N. Sinha, S. Goel, A.J. Joseph, H. Yadav, K. Batra, M.K. Gupta, B. Kumar, *Ceram. Int.* **44**, 8582 (2018)
27. S.J. Yang, C.R. Park, *Nanotechnology* **19**, 35609 (2008)
28. Y. Zhang, J. Chung, J. Lee, J. Myoung, S. Lim, *J. Phys. Chem. Solids* **72**, 1548 (2011)
29. Z. Yong-Zhe, W. Li-Hui, L. Yan-Ping, X. Er-Qing, Y. De, C. Jiang-Tao, *Chinese Phys. Lett.* **26**, 38201 (2009)
30. Z.L. Wang, X.Y. Kong, J.M. Zuo, *Phys. Rev. Lett.* **91**, 185502 (2003)
31. Z.W. Pan, Z.R. Dai, and Z. L. Wang *Science* (80). **291**, 1947 (2001)
32. Y.V. Kaneti, Z. Zhang, J. Yue, Q.M.D. Zakaria, C. Chen, X. Jiang, A. Yu, *Phys. Chem. Chem. Phys.* **16**, 11471 (2014)
33. P.X. Gao, Z.L. Wang, *J. Am. Chem. Soc.* **125**, 11299 (2003)
34. S. Kamba, V. Bovtun, J. Petzelt, I. Rychetsky, R. Mizaras, A. Brilingas, J. Banys, J. Grigas, M. Kosec, *J. Phys. Condens. Matter* **12**, 497 (2000)
35. S.A. Ansari, A. Nisar, B. Fatma, W. Khan, M. Chaman, A. Azam, A.H. Naqvi, *Mater. Res. Bull.* **47**, 4161 (2012)
36. H. Terauchi, Y. Yoneda, H. Kasatani, K. Sakaue, T. Koshiba, S. Murakami, Y. Kuroiwa, Y. Noda, S. Sugai, S. Nakashima, H. Maeda, *Jpn. J. Appl. Phys.* **32**, 728 (1993)
37. C.W. Zou, L.X. Shao, L.P. Guo, D.J. Fu, T.W. Kang, *J. Cryst. Growth* **331**, 44 (2011)
38. Dhananjay, S.B. Krupanidhi, *Appl. Phys. Lett.* **89**, 82905 (2006)
39. M.K. Gupta, B. Kumar, *J. Mater. Chem.* **21**, 14559 (2011)
40. S. Sagadevan, I. Das, K. Pal, P. Murugasen, P. Singh, *J. Mater. Sci. Mater. Electron.* **28**, 5235 (2017)
41. A.K. Jonscher, *Nature* **267**, 673 (1977)
42. R. Khan, S. Fashu, Zia-Ur-Rehman, *J. Mater. Sci. Mater. Electron.* **28**, 4333 (2017)
43. S. Sagadevan, K. Pal, Z.Z. Chowdhury, M.E. Hoque, *J. Sol-Gel. Sci. Technol.* **83**, 394 (2017)

44. N. Sinha, G. Ray, S. Godara, M.K. Gupta, B. Kumar, *Mater. Res. Bull.* **59**, 267 (2014)
45. R. Joshi, P. Kumar, A. Gaur, K. Asokan, *Appl. Nanosci.* **4**, 531 (2014)
46. R. Meyer, R. Waser, K. Prume, T. Schmitz, S. Tiedke, *Appl. Phys. Lett.* **86**, 142907 (2005)
47. A.J. Joseph, B. Kumar, *Solid State Commun.* **271**, 11 (2018)
48. A.J. Joseph, S. Goel, A. Hussain, B. Kumar, *Ceram. Int.* **43**, 16676 (2017)
49. J. Dhananjay, Nagaraju, S.B. Krupanidhi, *J. Appl. Phys.* **99**, 34105 (2006)